Automatic Design System With Generative Adversarial Network and Vision Transformer for Efficiency Optimization of Interior Permanent Magnet Synchronous Motor

Yuki Shimizu , *Member, IEEE*

Abstract—**Interior permanent magnet synchronous motors are becoming increasingly popular as traction motors in environmentally friendly vehicles. These motors, which offer a wide range of design options, require time-consuming finite-element analysis to verify their performance, thereby extending design times. To address this problem, in this article, we propose a deep learning model that can accurately predict the iron loss characteristics of different rotor topologies under various speed and current conditions, resulting in an automatic design system for the internal permanent magnet synchronous motor rotor core. Using this system, the computation time for efficiency maps is reduced to less than 1/3000 of the time required for finite-element analysis. The system also shows efficiency optimization results similar to the best results of previous research while reducing the computational time for optimization by one or two orders of magnitude.**

Index Terms—**Design optimization, generative adversarial network (GAN), iron loss, permanent magnet (PM) motors, vision transformer (ViT).**

I. INTRODUCTION

IN THE current era, the increasing integration of electrical and mechanical elements in a wide range of goods, along with the development of sustainable energy sources, such as wind power generation, is being promoted to achieve carbon neutrality. As a result, the demand for machines that efficiently convert electrical power into mechanical action has increased dramatically. In the automotive industry, for example, there has been a remarkable global increase in the number of electric transportation systems, including electric cars, plug-in hybrid vehicles, and fuel cell units, along with the emergence of interior permanent magnet synchronous motors (IPMSMs), which are

replacing internal combustion engines as the primary drive system in these electrified modes of transportation. In anticipation of continued growth in motor use in the future, improving the efficiency of IPMSMs remains a critical challenge.

The design phase of today's IPMSMs is prolonged due to two critical factors. First, the widespread use of finite-element analysis (FEA) to calculate the characteristics of IPMSMs. Second, the wide range of design alternatives in these motors, including parts, such as permanent magnets (PMs) and flux barriers, forces the iterative evaluation of numerous configurations to achieve defined standards. These combined factors lead to longer development times in IPMSM design, with multiple structures subjected to FEA and development based largely on the trial-and-error approach taken by designers.

Many studies have been conducted to reduce the time required for the optimal design of advanced IPMSMs by implementing machine learning (ML) methods [1], [2], [3], [4], [5], [6], [7], [8], [9], [10], [11], [12], [13], [14], [15], [16], [17]. Although ML-focused research requires a certain amount of training time, the computation takes less than 1/1000th of the time compared with FEA upon model completion [15]. Previous studies can be divided into those that use geometric parameters as input and those that use topology information. The former method takes the dimensions and current conditions of the motor design as input and predicts the motor characteristics with high accuracy. The dimension of the input information is often fixed, and the applicable domain of the ML model is based on the initial geometry, making the method suitable after the conceptual design is completed. The latter approach interprets the material data under the polar coordinate of the rotor geometry for IPMSMs as tensors, allowing the use of deep learning (DL) image processing models, such as convolutional neural networks (CNNs) and vision transformers (ViTs). Although this method is capable of handling multiple topologies, it results in an increase in training dataset size, model dimensions, and training time.

The above-mentioned studies encounter limitations in input features, such as geometry type, current and speed conditions, and model output variables, such as torque and efficiency, which hinder the construction of a comprehensive automatic design system for IPMSMs. Therefore, this study proposes a DL model capable of handling various input and output conditions, thus
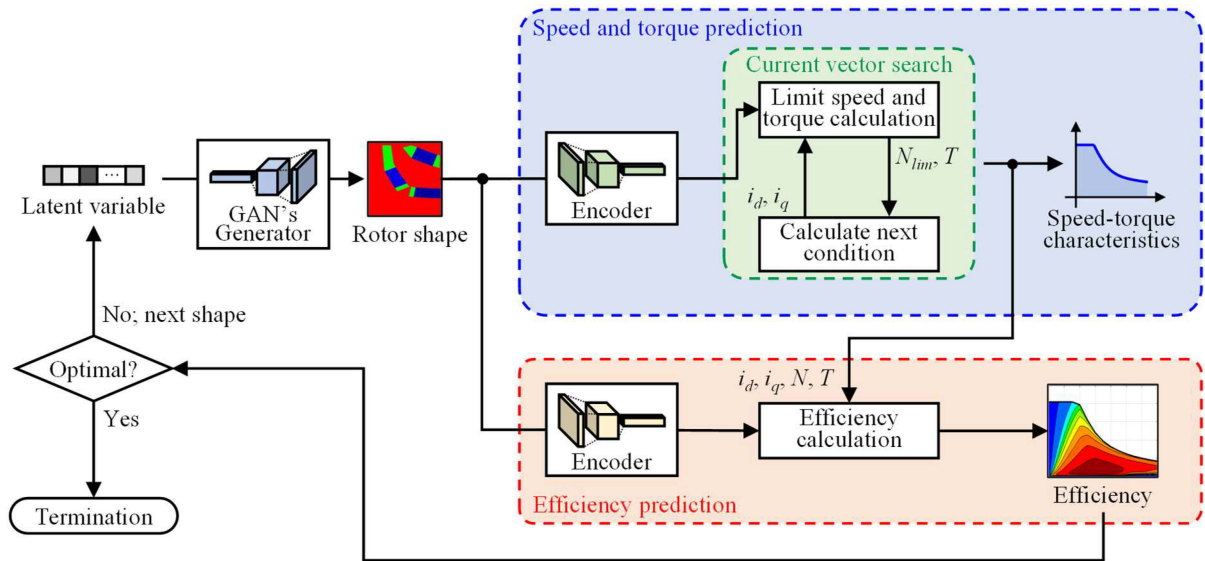
Fig. 1. Overall configuration of the automatic design system for efficiency optimization. The blue part represents the prediction for the speed and torque characteristics using the model proposed in [17]. The red part represents the prediction for the iron loss characteristics, which is described in detail in Sections III-C and IV. i_d and i_q are the d- and q-axis currents, respectively, N is the motor speed, $N_{\lim}$ is the limit motor speed, and T is the torque.

contributing to the development of an automatic design system for IPMSMs, as shown in Fig. 1. The system uses a generative adversarial network (GAN), a type of deep generative model, to construct the rotor shape of IPMSMs and promptly predicts the speed, torque, and iron loss characteristics using two different characteristic prediction models. Configured to include current and speed conditions in addition to rotor geometry data, these models enable fast, high-quality efficiency map generation during current vector control, such as maximum torque per ampere (MTPA) control and flux-weakening (FW) control. This approach allows efficiency optimization for numerous rotor topologies at any speed and torque setting. The proposed system also has the advantage that the optimization can be repeated many times after the training phase is completed. The main contributions of this study are as follows.

1) The construction of a model that accurately predicts iron loss characteristics in IPMSMs with three different rotor topologies.
2) To propose a time-efficient automatic design system for motor efficiency at arbitrary speed and torque points.
3) To validate the reliability of the automatic design through FEA and prototype experimentation on the optimal geometry generated by the design system.

The dataset described in Section IV-A is available at IEEE DataPort [18]. This article is a revised version of a conference proceeding [19] with additions regarding the details of the DL model and the results of prototype experiments.

II. RELATED WORKS

A. Design Optimization Without ML

Several studies have developed algorithms to efficiently determine the most appropriate design. Farhadian et al. [20] formulated an optimization mechanism, based on an improved particle swarm optimization, to enrich the torque aspects of a synchronous reluctance motor (SynRM). Son et al. [21] improved the rotor arrangement of an IPMSM with grain-oriented electrical steel in the stator teeth by applying a revised genetic algorithm. Das et al. [22] performed a sensitivity analysis on the noise vibration performance of the permanent magnet synchronous motor (PMSM) for ten geometric parameters and performed design optimization for the highly sensitive parameters. Pfister et al. [23] proposed a method to perform an optimization of a PMSM assuming linear magnetic material properties, followed by FEA optimization with a small number of generations. Although these methods effectively optimize the geometry, they determine the motor characteristics only at a single or a small number of current settings, making them unsuitable for IPMSMs operating over wide current ranges, such as those used in automotive applications.

B. Shape Optimization With ML

To accelerate shape optimization, several research efforts have used ML to construct surrogate models as an efficient replacement for FEA. By using these surrogate models, we can perform the design of IPMSMs with a reduced reliance on FEA iterations, or potentially, without FEA at all. Islam et al. [1] used response surface methodology to optimize a pair of rotor design parameters at multiple output points of an IPMSM using the response surface methodology. Zheng et al. [2] performed multiobjective refinement of an IPMSM installed with rare Earth PMs and ferrite PMs using the response surface methodology. Sun et al. [3] classified the geometric parameters of an IPMSM into three different groups using cross-factor variance analysis and optimized them in terms of torque and loss characteristics by applying kriging. Sun et al. [4] proposed a sequential subspace optimization technique using the kriging

method for a PM hub motor, respectively. Dhulipati et al. [5] used support vector regression to develop a predictive model for a six-phase IPMSM. Hao et al. [6] developed a model to identify the relationship between design parameters and torque ripple in an IPMSM using radial basis function networks and used this model for optimization. Yan et al. [7] constructed a surrogate model using an artificial neural network for an IPMSM with a cage conductor embedded in the rotor and performed multiobjective optimization of torque, inertia, efficiency, power factor, and cogging torque. Zheng et al. [8] proposed an optimization method that combines ridge regression and the whale optimization algorithm for PM synchronous linear motors. Pan and Fang [9] used XGBoost, a superior distributed gradient boosting library, to understand the relationship between the torque characteristics and the structural parameters of PM arc motors, and then used this model for optimization. Kwon and Lim [10] trained a surrogate model that learned the relationship between motor characteristics and structural parameters of a PM-assisted SynRM using a random forest and optimized the design using a genetic algorithm. Despite the demonstrated effectiveness of these ML-based surrogate models for automated IPMSM design, their ability to deal with geometric parameters within the same dimension is limited, restricting them to certain limited geometries.

C. Topology Optimization With DL

Various research efforts have introduced rotor design using topology optimization and DL. Barmada et al. [11] considered the incorporation of DL technology to optimize the rotor core topology of the SynRM. Sasaki et al. [12] accelerated the rotor topology optimization of IPMSM with a CNN trained from the analysis of the magnetic flux distribution at the initial position and the material distribution. Sato and Igarashi [13] predicted motor parameters from rotor geometry using CNNs and used the results to evaluate individuals in topology optimization. Khan et al. [14] optimized the topology of the SynRM rotor using deep reinforcement learning, a less biased approach to topology optimization compared with supervised learning. These research efforts are primarily focused on identifying innovative rotor designs and do not consider the wide operational range of properties and iron loss characteristics required for applications, such as automotive settings.

III. AUTOMATIC DESIGN SYSTEM

A. Target Motor

The method proposed in this study is not limited to any specific application. To validate the generality of the proposed method, the following discussion focuses on automotive IPMSM, which requires a wide operating range. Fig. 2 shows the rotor topology of three typical automotive traction motors used in this study. All IPMSMs have 8-pole, 48-slot stators with distributed windings. Further specifications of each model can be found in [24] and [25].
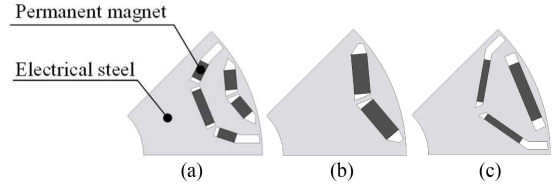

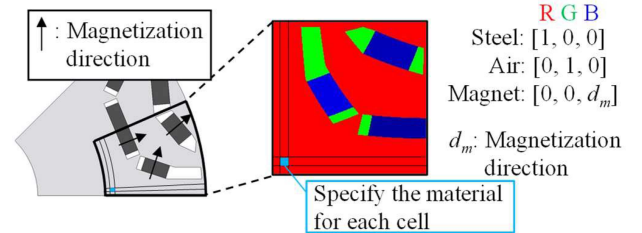Fig. 2. Single-pole conventional rotor shapes. (a) Two-dimensional. (b) V. (c) Nabla.

Fig. 3. Schematic of material representation of rotor shape.

B. Motor Design by Deep Generative Model

This study focuses on different rotor topologies and tries to handle them in a harmonious way by representing rotor geometries as images. Fig. 3 shows a schematic of the material representation approach implemented in the system. The rotor pole coordinates are specified as electrical steel sheets, PMs, or air. The image represents the rotor configuration by assigning one-hot vectors to the 256×256 RGB pixels for each of the three materials, as shown in the right part of Fig. 3. A GAN generates the rotor image from a 256-dimensional (256-D) latent variable space as follows:

$$\mathbf{x} = \mathcal{G}(\mathbf{z}) \tag{1}$$

where $\mathcal{G}$ is the generator of the GAN, $\mathbf{x}$ is the generated rotor image, and $\mathbf{z}$ is the latent variable. See [17] for more details.

C. Prediction Models

By predicting the characteristics from the generated images, an automatic design system can be constructed without FEA integration. This study uses geometry, current, and speed conditions as input data, and considers models for predicting motor parameters and iron loss as follows:

$$\Psi_a, L_d, L_q = \mathcal{E}_1(\mathbf{x}, i_d, i_q) \tag{2}$$

$$W_h, W_e = \mathcal{E}_2(\mathbf{x}, i_d, i_q, N) \tag{3}$$

where $\mathcal{E}_1$ and $\mathcal{E}_2$ are the prediction models for motor parameters and iron loss, respectively, Ψ_a is the PM flux linkage, L_d and L_q are the d- and q-axis inductances, respectively, i_d and i_q are the d- and q-axis currents, respectively, N is the motor speed, and W_h and W_e are the hysteresis loss and eddy current loss, respectively.

These models allow the prediction of torque and efficiency aspects under various current vector control conditions as follows:

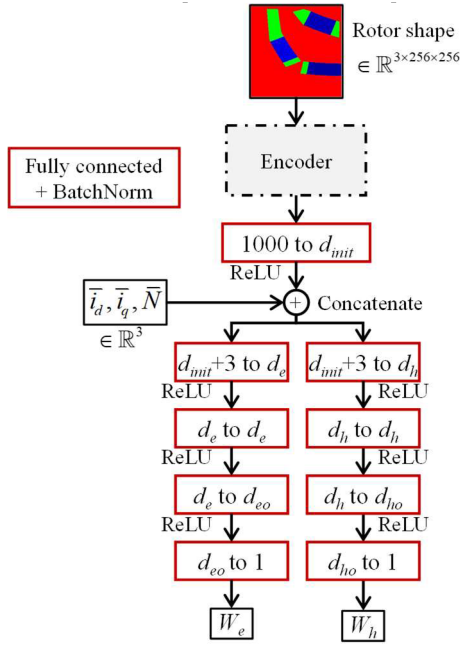$$T = P_n \{\Psi_a i_q + (L_d - L_q) i_d i_q\} \tag{4}$$

Fig. 4. Common architecture of iron loss prediction model.

$$\eta = \frac{\omega_m T - W_i}{\omega_m T + R_a I_a^2} = \frac{\omega_m T - (W_h + W_e)}{\omega_m T + R_a I_a^2} \quad (5)$$

where P_n is the number of pole pairs, R_a is the winding resistance, I_a is the magnitude of the armature current vector, ω_m is the mechanical angular frequency, and W_i is the iron loss.

The model proposed in [17] is used for motor parameter prediction, and the iron loss prediction model is detailed in this section. Fig. 4 shows the common architecture of the iron loss prediction model used in this study, where d_{init} is the dimension of the encoded shape components, d_h and d_e are the dimensions of the hidden layers of the multilayer perceptron (MLP) for hysteresis loss and eddy current loss prediction, respectively, and d_{ho} and d_{eo} are the dimensions of the second layer from the end of the MLP for hysteresis loss and eddy current loss prediction, respectively. FEA conditions, d- and q-axis currents, and motor speed are standardized according to the following equations:

$$\bar{X} = \frac{X - \mu_X}{\sigma_X} \quad (X \in \{i_d, i_q, N\}) \quad (6)$$

where μ_X and σ_X are the mean and standard deviation of the training data, respectively.

As input, a trained model that encodes the rotor image generated by the GAN is used to extract the semantic rotor geometry data from the image. The resulting shape encoding information is combined with the FEA operating conditions in a multitask learning context, allowing simultaneous prediction of hysteresis loss and eddy current loss. The MLP consists of fully connected layers and batch normalization, with a rectified linear unit serving as the activation

$$Z^{(l+1)} = \phi \left(BN_{\gamma^{(l)},\beta^{(l)}} \left(W^{(l)} Z^{(l)} + B^{(l)} \right) \right) \quad (7)$$

$$BN_{\gamma^{(l)},\beta^{(l)}} \left(X^{(l)} \right) = \gamma^{(l)} \frac{X^{(l)} - E\left[X^{(l)}\right]}{\sqrt{\text{Var}\left[X^{(l)}\right] + \varepsilon}} + \beta^{(l)} \quad (8)$$

$$\phi \left(X^{(l)} \right) = \text{ReLU} \left(X^{(l)} \right) = \max \left(X^{(l)}, 0 \right) \quad (9)$$

where $Z^{(l)}$ is the input to the l-layer, and $W^{(l)}$ and $B^{(l)}$ are the weights and biases of the l-layer to be trained. In the batch normalization, the mean and standard deviation are computed per dimension over the minibatches, $\gamma^{(l)}$ and $\beta^{(l)}$ are the learnable parameter vectors, and $\varepsilon = 0.00001$ is a constant added to the minibatch variance for numerical stability.

IV. TRAINING OF IRON LOSS PREDICTION MODEL

A. Dataset and Training Setting

To accommodate the large data requirements of DL, this study combines computer-aided design (CAD) and FEA for dataset generation. In terms of geometry, 30 000 shapes were formulated for each topology by randomly generating geometric parameters based on the three rotor topologies, as shown in Fig. 2. For these geometries, random FEA conditions, such as phase current (0–140 Arms), current phase (0°–90°), and motor speed (0–15 000 r/min), were also generated, resulting in 90 000 FEA cases across the three rotor topologies. The motor characteristics to be calculated included core iron losses, specifically hysteresis and eddy current losses. The iron loss calculation was based on the fast Fourier transform of the magnetic flux density and material data sheets. JMAG-Designer 19.1 software was used for analysis, yielding 85 184 datasets after excluding failed cases. See [16] for details.

A total of 80% of the dataset was used for training, while the remaining 20% was used for validation. The mean squared error determined the loss function for multitask learning, as shown in the following equation:

$$\mathcal{L} = \mathcal{L}_h + \mathcal{L}_e = \frac{1}{n} \left(\sum_{i=1}^{n} \left(W_h^{(i)} - \hat{W}_h^{(i)} \right)^2 + \sum_{i=1}^{n} \left(W_e^{(i)} - \hat{W}_e^{(i)} \right)^2 \right) \quad (10)$$

where $W_h^{(i)}$ and $\hat{W}_h^{(i)}$ are the predicted hysteresis loss and training data, respectively, and $W_e^{(i)}$ and $\hat{W}_e^{(i)}$ are the predicted eddy current loss and training data, respectively.

The number of training epochs was set to 100. The optimizer was Adam, and the batch size was set to 128. PyTorch was used to implement the neural network model.

B. Hyperparameter Optimization

Hyperparameter optimization was performed on the iron loss prediction model, as shown in Fig. 4. The procedure started by using the tree-structured Parzen estimator (TPE) for hyperparameter optimization. Table I lists the variables to be optimized along with their upper and lower bounds, where n_l is the number of hidden layers in the MLP, and lr is the learning rate of the optimizer. The Optuna library was used for the TPE [26]. During each optimization evaluation, a set of 20 epochs was assigned.

TABLE I
HYPERPARAMETERS FOR IRON LOSS PREDICTION MODEL

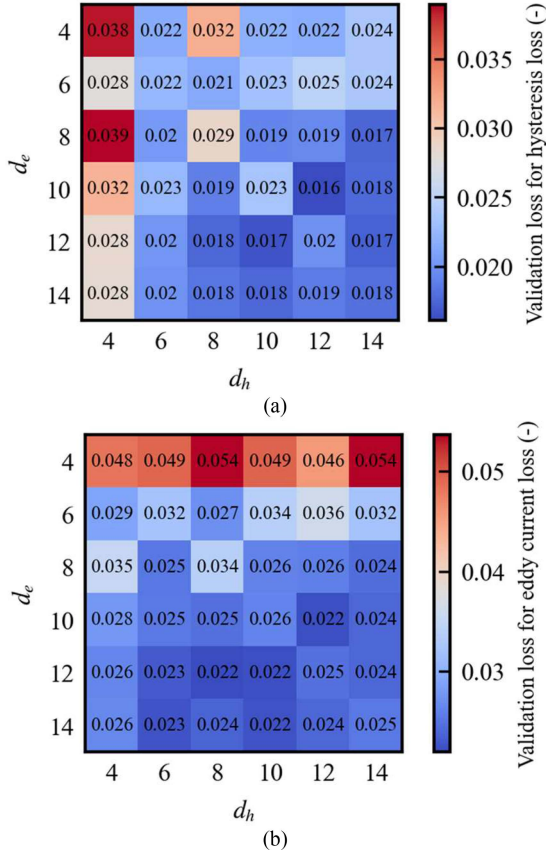| Symbols	Range	Selected by TPE
d_{init}	(2, 12)	8
d_h	(5, 55)	15
d_e	(5, 55)	10
d_{ho}	(10, 100)	50
d_{eo}	(10, 100)	50
n_l	(3, 11)	3
lr	(0.00001, 0.1)	0.0004

Fig. 5. Validation loss differences for several d_h and d_e combinations for (a) hysteresis loss and (b) eddy current loss. The mean values for ten training runs are shown.
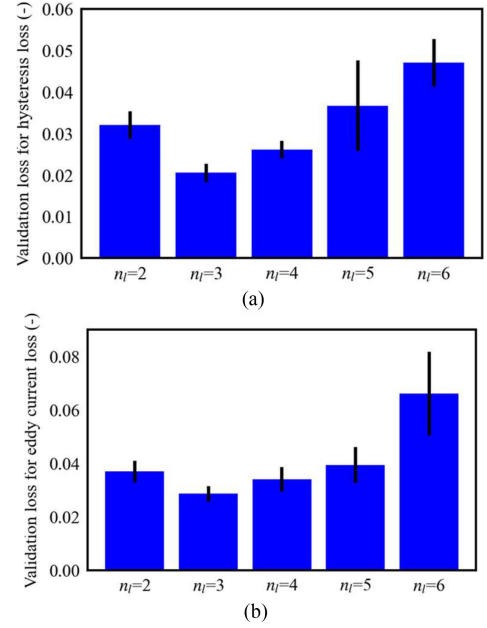

Fig. 6. Validation loss for different n_l for (a) hysteresis loss and (b) eddy current loss. The mean and standard deviation values for ten training runs are shown.

The encoder model was the pretrained Swin Transformer (Swin-T) [27], and the optimization results are shown in Table I.

Further comparative evaluations were performed based on the optimized hyperparameters of TPE. One focus was the comparison of hidden layer sizes in MLPs. Fig. 5 shows the validation loss differences for several d_h and d_e combinations, where the validation losses are evaluated at the end of the 100th training epoch and the listed validation losses are the mean values over 10 training runs. For $d_h = 4$, there is a significantly high validation loss for the hysteresis loss, which materializes independently of the d_e values, decreasing and reaching equilibrium as d_h increases. A parallel trend appears for the eddy current loss and d_e, indicating that an adequate representation of the nonlinearity within the iron loss characteristics occurs when the hidden layer

dimensions exceed 10. In the following steps, $(d_h, d_e) = (12, 10)$ is used because it produced the minimum validation losses for both hysteresis and eddy current losses.

Fig. 6 shows the validation loss for different n_l values to compare the influence of the number of hidden layers in MLPs. The lowest validation loss for both hysteresis and eddy current loss is achieved with $n_l = 3$, and it increases as the number of layers increases beyond 3. This result suggests that it may not be necessary to rely on highly nonlinear models to predict iron loss from the encoded geometry data, motor speed, and current conditions. This is also supported by Steinmetz's experimental law [28], which states that the nonlinearity of hysteresis and eddy current loss is affected by up to a power of 1–2 with respect to the frequency (associated with speed) and the maximum flux density value (associated with current).

The evaluation of the shape encoder models is performed subsequently. Fig. 7 shows the validation loss associated with the weights of the Swin-T encoder weights, where "pretrained" represents the encoder pretrained using ImageNet [29], and "normal" represents the model without pretraining. The contrast between "fix" and "train" refers to whether the encoder weights are fixed or additionally trained when training with the iron loss dataset. When comparing the validation loss, the observed minimum validation loss for both hysteresis loss and eddy current loss is achieved using a fixed weight encoder with pretraining.

Finally, the pretrained models were compared. Table II lists the validation loss of several well-known encoder models [27], [30], [31], [32], [33]. The final comparative evaluation shows that the Swin-T model produces the minimum validation loss, making it the most appropriate encoder model for this study.

Fig. 8 shows the prediction results of the optimized iron loss prediction model for the test data, where the test data are
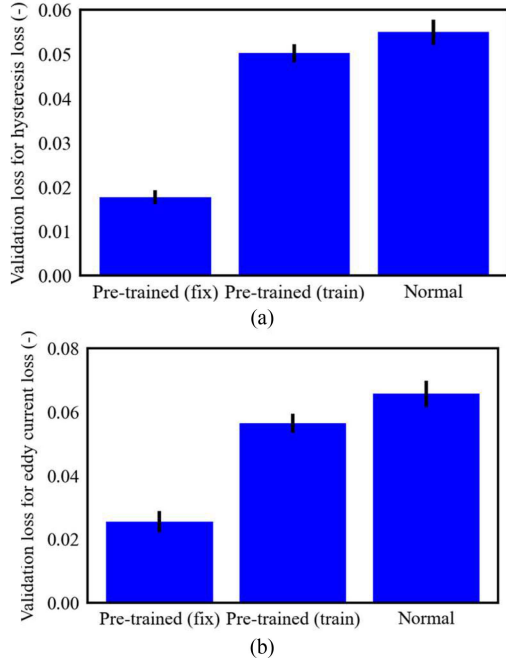
Fig. 7. Validation loss for different types of training for (a) hysteresis loss and (b) eddy current loss. The mean and standard deviation for ten training runs are shown. "Pretrained" represents the pretrained encoder, and "normal" represents the model without pretraining. The contrast between "fix" and "train" refers to whether the encoder weights are fixed or additionally trained when training with the iron loss dataset.

TABLE II
VALIDATION LOSSES FOR DIFFERENT ENCODERS

Model	Validation loss for W_h	Validation loss for W_e
ResNet-18 [30]	0.0539 ± 0.0117	0.0401 ± 0.0084
ResNet-34 [30]	0.0456 ± 0.0035	0.0369 ± 0.0114
ResNet-50 [30]	0.0562 ± 0.0145	0.0428 ± 0.0128
ResNet-101 [30]	0.0567 ± 0.0126	0.0447 ± 0.0050
ResNet-152 [30]	0.0570 ± 0.0050	0.0481 ± 0.0085
VGG-11 (w/bn) [31]	0.0289 ± 0.0025	0.0216 ± 0.0018
VGG-13 (w/bn) [31]	0.0267 ± 0.0018	0.0218 ± 0.0020
VGG-16 (w/bn) [31]	0.0357 ± 0.0089	0.0272 ± 0.0018
VGG-19 (w/bn) [31]	0.0310 ± 0.0034	0.0267 ± 0.0019
ViT-B/16 [32]	0.0429 ± 0.0051	0.0287 ± 0.0037
ViT-B/32 [32]	0.0348 ± 0.0064	0.0292 ± 0.0037
ViT-L/16 [32]	0.0346 ± 0.0042	0.0268 ± 0.0035
ViT-L/32 [32]	0.0378 ± 0.0053	0.0317 ± 0.0027
Swin-T [27]	$\mathbf{0.0267 \pm 0.0033}$	$\mathbf{0.0177 \pm 0.0011}$
Swin-B [27]	0.0406 ± 0.0092	0.0279 ± 0.0027
Poolformer-s12 [33]	0.0577 ± 0.0084	0.0428 ± 0.0104

*mean ± std for ten training runs.
The bold values is used to emphasize good results.

additional 600 datasets of 200 FEA results for each topology. The optimized prediction model was found to achieve highly accurate predictions even for unknown FEA data.

V. EFFICIENCY OPTIMIZATION

The combination of the models, as described in Section IV, results in the automatic design system for the IPMSM rotor core, as shown in Fig. 1. Using this design system, the efficiency optimization design is performed within the constraints of the 256-D latent variable space found in the generative model.
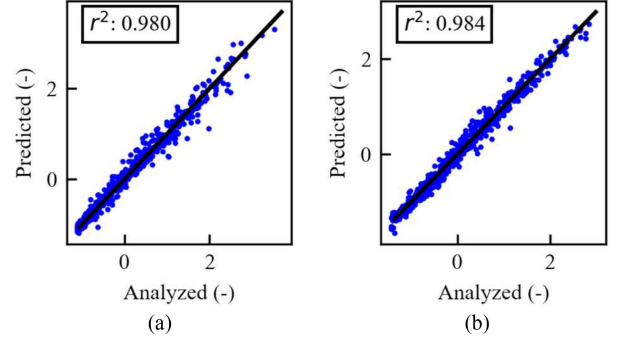

Fig. 8. Prediction results for test data of optimized iron loss prediction model (a) for hysteresis loss and (b) for eddy current loss. r^2 indicates the coefficient of determination (higher is better). "Analyzed" indicates the results of the FEA, while "Predicted" indicates the predicted results of the prediction model.
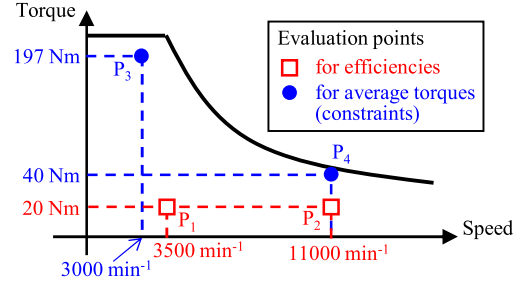

Fig. 9. Evaluation points used for optimization. The blue points are for efficiency evaluation. The red squares are for average torque constraints.

A. Problem

In this study, the efficiency maximization design is performed at two unique evaluation points, constrained by two torque limits, as shown in Fig. 9. The efficiency maximization problem, incorporating a torque constraint for the IPMSM, is formulated as follows:

$$\min_{\mathbf{z}} \quad \left(-\frac{\eta_1^{\text{pred}}}{\eta_1^{\text{init}}}, -\frac{\eta_2^{\text{pred}}}{\eta_2^{\text{init}}} \right)^T$$
$$\text{s.t.} \quad g_i : T_i^{\text{pred}} \geq \alpha T_i^{\text{req}} \quad (i = 3, 4) \tag{11}$$

where η_1^{pred} and η_2^{pred} are the predicted efficiencies at operating points P_1 (3000 r/min, 20 N·m) and P_2 (11 000 r/min, 20 N·m), with each value normalized by the initial values η_1^{init} and η_2^{init}, respectively. The constraint conditions g_i are the torque constraints for two required operating points P_3 (3500 r/min, 197 N·m) and P_4 (11 000 r/min, 40 N·m), with a coefficient ($\alpha = 1.05$) to account for the prediction error. The efficiency evaluation points are determined based on the motor operating points in the worldwide harmonized light vehicles test cycle (WLTC). The complete WLTC loss calculation procedure is described in [16]. Two other torque constraints are set to maintain the same characteristics as the reference motor [16].

Average torques, used in the efficiency evaluation and torque constraint analysis, were calculated using the motor parameter
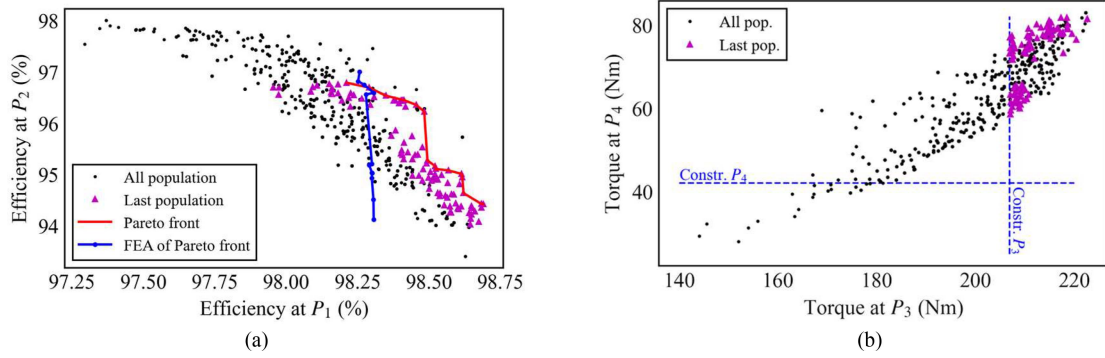
Fig. 10. Optimization result for (a) efficiencies and (b) torques using the proposed automatic design system. The solid red line represents the Pareto front in the last generation. Individuals outside the Pareto front were eliminated in the optimization process because they did not satisfy the torque constraint. The solid blue line represents the result of the FEA performed on the individuals in the Pareto front.
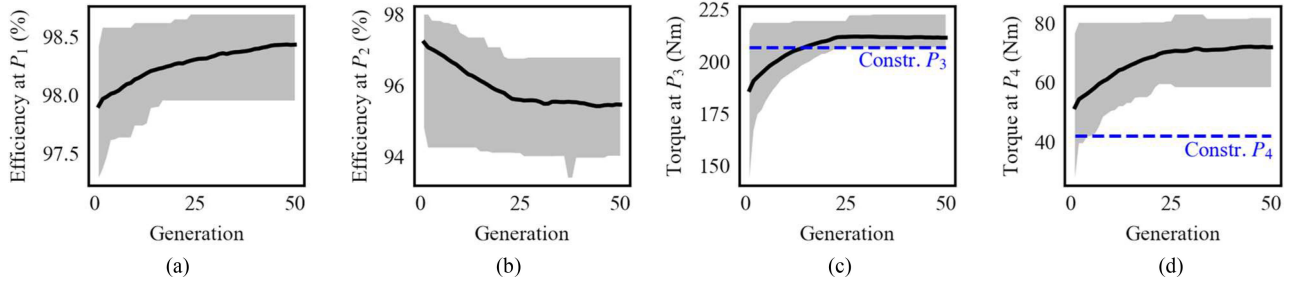

Fig. 11. Changes in the evaluation values of (a) and (b) efficiencies and (c) and (d) torques during the optimization process. The solid black lines indicate the mean values for each population, and the gray areas indicate the maximum to minimum values.

prediction model [17]. Current conditions for torque and efficiency calculations were determined by MTPA control and FW control algorithm [30].

NSGA-II [34] was used as the optimization algorithm, and the pymoo [35] library was used for implementation. The population size was 100, and the number of offspring was 10. Latin hypercube sampling was used for sampling the initial population, the tournament method was used for selection, the simulated binary crossover was used for crossover, and polynomial mutation was used for mutation. The termination condition was set to 50 generations.

B. Optimization Results

Fig. 10 shows the efficiency characteristics and torques at required speeds for all individuals in the optimization process. Fig. 11 shows the changes in the evaluation values during the optimization process, and Fig. 12 shows the Pareto solution shapes. After optimization, the final generation population established a clear Pareto front in terms of efficiencies. Notably, the entire final generation population satisfied the torque constraints, specifically the operating point constraint related to maximum torque was active, as shown in Fig. 11(c). Although the efficiency at high speed P_2 decreased during the optimization process, this was due to the survival of individuals with increased magnetic
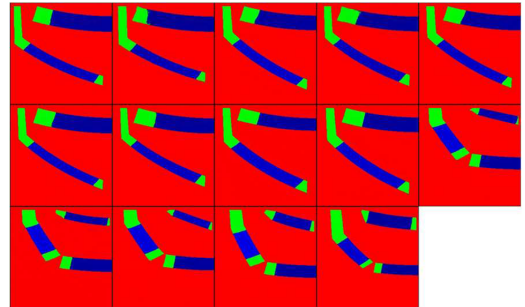

Fig. 12. Shapes of all Pareto solutions of optimization, which are indicated by the red line in Fig. 10(a).

flux linkages and increased iron loss in order to prioritize satisfying the maximum torque constraint. The final generation population is divided into two main clusters, representing Nabla and 2-D topologies, as shown in Fig. 12. Nabla generally produces higher torque at low speed due to the proximity of the PMs to the gap, which reduces copper loss and increases efficiency at P_1. In contrast, the 2-D topology is designed to mitigate gap flux density harmonics and preferentially achieves higher efficiency at high speeds P_2, where iron losses dominate.

Efficiency predictions for the Pareto front are usually better than those obtained from FEA because tradeoff optimization with surrogate models tends to converge on individuals with

| Item (unit) | Proposed | Parameter optimization (w/XGBoost) [16] | | |
		2D	V	Nabla
Loss under WLTC (FEA) (kJ)	**263.8**	**266.3**	329.7	311.7
− Copper loss (kJ)	199.1	206.1	232.0	229.3
− Iron loss (kJ)	64.7	60.2	97.7	82.4
Computation time for optimization (min)	**3.783 ± 0.037**	123.58 ± 0.13	55.25 ± 0.84	89.30 ± 0.23

The bold values is used to emphasize good results.
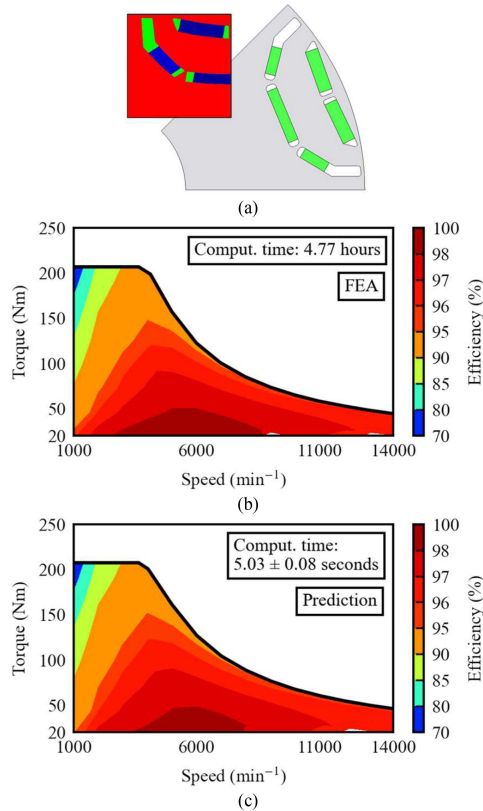

(a)

(b)

(c)

Fig. 13. Efficiency maps for selected optimal design. (a) Selected rotor geometry and efficiency maps calculated by (b) FEA and (c) automatic design system.

Fig. 14. Photographs of prototype. (a) Stator core. (b) Rotor core.

Device	Manufacturer
Torque detector (SS-500)	Ono Sokki Co., Ltd., Yokohama, Japan
16-kW induction motor (Load)	Fuji Electronic Co., Ltd., Tokyo, Japan
PWM inverter	Myway Plus Co., Yokohama, Japan

overestimated solutions [15]. Nevertheless, the difference between the system predictions and the FEA results is marginal, highlighting the effectiveness of the system in predicting efficiencies with high accuracy. The efficiency prediction error at P_1 may appear large, but this is due to the more detailed scaling of the horizontal axis in Fig. 10(a) as opposed to the vertical axis, which actually results in a small prediction error.

To evaluate the efficiency characteristics in detail, the individual with the highest efficiency at P_2 was selected from among the Pareto solutions. Fig. 13 shows the selected rotor geometry and the efficiency maps calculated by FEA and system prediction. The prediction accuracy of the efficiency characteristics is high, and the prediction system reduces the computational time required, with evaluations performed over ten iterations using a computer with an Intel Core i7-9700K CPU, 32.0 GB of RAM, and an NVIDIA GeForce RTX 3090 SUPER (24 GB) GPU.

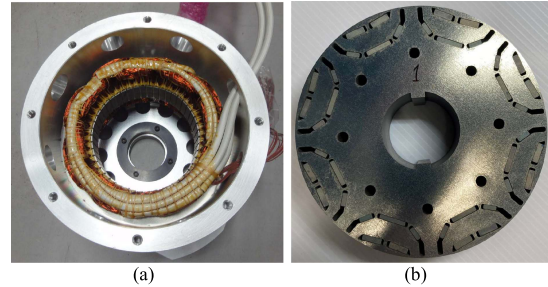The optimization performance is further evaluated against previously proposed methods [16], namely parameter optimization with ML using XGBoost to predict torque and efficiency with geometric parameters of each topology. Table III presents a comparison of the losses of the optimized geometry under WLTC and the computational time for the optimization, where both methods were trained by the same training dataset, and the WLTC losses were only evaluated during powering. An analysis of the results shows that the converging geometry of the proposed method has similar loss characteristics with the best result of previous parameter optimization approaches. Moreover, the computational time for optimization is reduced by one or two orders of magnitude due to the implementation of parallel processing on GPUs.

C. Experimental Validation

Finally, a prototype of the optimized geometry, as shown in Fig. 13(a), was fabricated for experimental validation of the proposed system. Fig. 14 shows the fabricated prototype rotor shape with minor adjustments to the PM positioning shape and the fillet pattern. Table IV lists the experimental devices. A pulsewidth modulation (PWM) inverter with a carrier frequency of 10 kHz and a dc-side voltage of 650 V drove the tested IPMSMs. The load motor rating limits the speed to 6000 r/min. Due to equipment limitations, we measured the motor characteristics only in the low phase current range of 20 A or less.

Fig. 15 shows the no-load induced voltage, which is the line voltage between the U and V phases at 1200 r/min. The measured results are similar to the FEA results.
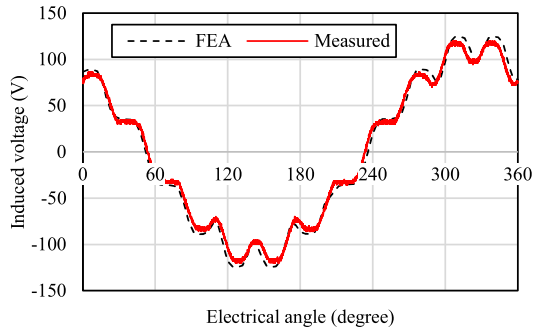
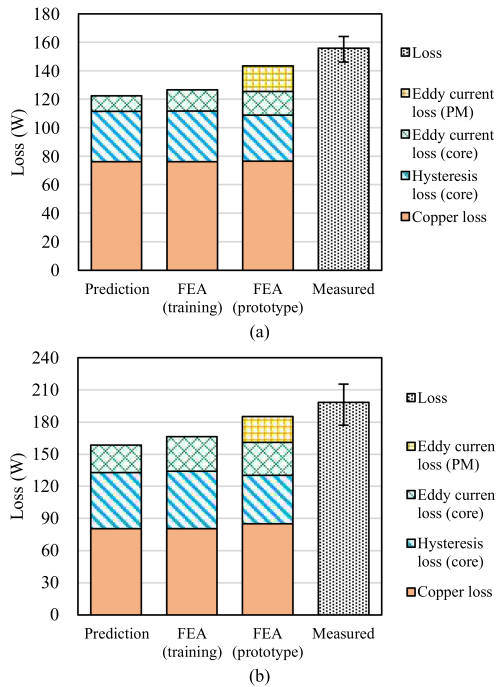Fig. 15. Measured no-load induced voltage at 1200 r/min.

Fig. 16. Measured loss characteristics (a) at 3500 r/min and 20 N·m and (b) at 5500 r/min and 20 N·m.

Fig. 16 shows the loss characteristics of the motor at 3500 r/min and 20 N·m and at 5500 r/min and 20 N·m, where the measured loss was calculated by subtracting the measured mechanical output and the electrical input to the motor, taking into account the premeasured mechanical losses. "FEA (training)" represents an analysis result performed under conditions identical to the training dataset of the proposed system, while "FEA (prototype)" represents an analysis result performed under conditions adapted to the actual experiment. Specifically, the "FEA (prototype)" geometry adopts the same CAD data used in the prototype drawings, including PM positioning shapes and fillets. In addition, it uses a finer analysis mesh and resolution, temperature condition, eddy current loss analysis in the PM, and current input, including carrier harmonics by PWM inverter. The current waveform, including the PWM harmonics, was analyzed by using MATLAB/Simulink and the JMAG-RT model.

Direct comparisons between the measured losses and system predictions indicate significant errors. On the other hand, comparing the system predictions with the FEA results under

conditions equivalent to the training data shows a prediction error of 3.5%, indicating a high level of accuracy in the system prediction itself. This leads to the conclusion that the discrepancy between the measured losses and the system predictions is due to the modeling errors present in the FEA results of the training dataset. Although the losses of "FEA (prototype)" were closer to the measured results than those of "FEA (training)," there are still differences between FEA and measured results due to factors, such as 3-D iron losses, stray load losses, manufacturing tolerances, and variations in machine losses. In addition, the analysis time for "FEA (prototype)" exceeded that of "FEA (training)" by more than 60 times.

VI. DISCUSSION AND LIMITATION

Big data are essential for DL, and high-quality training data are important to further improve the proposed system. For example, the coefficient of determination for the model, as shown in Fig. 8, had not reached 1. However, this result does not necessarily lead to the conclusion that the model simply needs to be improved. Because the training data were generated by FEA, errors can occur due to iterative calculations and poor mesh quality from automated multicase analysis. If the data contain a lot of noise, the prediction accuracy of the test data will never be 100%. Thus, the quality of the dataset has a significant impact on the investigation of the prediction model, and generating high-quality datasets is just as important as building a highly accurate model.

Also, the tradeoff between the quality and quantity of the training dataset is important for the proposed system. The result of the loss comparison in Fig. 16 leads to the conclusion that the more detailed FEA results are closer to the measured results. However, as the accuracy of FEA improves, the analysis time increases. Because the applicability of the proposed system depends essentially on the training dataset, the tradeoff between modeling accuracy and FEA analysis time limits the construction of a DL model that covers a wider range of applications. There are many more design variables and output characteristics to consider in motor design than those covered in this study, so it is necessary to quantitatively discuss how many datasets are required for a given model application range, and this is future work.

VII. CONCLUSION

In this article, we proposed a DL model that accurately predicts the iron loss characteristics in IPMSMs with three different rotor topologies under various speeds and current conditions. In addition, the combination of this model and previously proposed models resulted in an automatic design system for the IPMSM rotor core. Using this system, the computation time for efficiency maps was less than 1/3000 that of the FEA. In addition, the efficiency optimization results with this system showed the same level of performance as the best results of the previous studies, while the computation time for optimization is reduced by one or two orders of magnitude.

The proposed system, which is not limited to a specific application, is available for different motor specifications by

changing the optimization settings and electrical parameters. In addition, it has the capacity for repeated optimizations once the training phase is completed, and it also can respond to minor adjustments in the requirements.

ACKNOWLEDGMENT

REFERENCES

[1] M. S. Islam, M. Chowdhury, A. Shrestha, M. Islam, and I. Husain, "Multiload point optimization of interior permanent magnet synchronous machines for high-performance variable-speed drives," *IEEE Trans. Ind. Appl.*, vol. 57, no. 1, pp. 427–436, Jan./Feb. 2021.

[2] S. Zheng, X. Zhu, L. Xu, Z. Xiang, L. Quan, and B. Yu, "Multi-objective optimization design of a multi-permanent-magnet motor considering magnet characteristic variation effects," *IEEE Trans. Ind. Electron.*, vol. 69, no. 4, pp. 3428–3438, Apr. 2022.

[3] X. Sun, Z. Shi, G. Lei, Y. Guo, and J. Zhu, "Multi-objective design optimization of an IPMSM based on multilevel strategy," *IEEE Trans. Ind. Electron.*, vol. 68, no. 1, pp. 139–148, Jan. 2021.

[4] X. Sun, N. Xu, and M. Yao, "Sequential subspace optimization design of a dual three-phase permanent magnet synchronous hub motor based on NSGA III," *IEEE Trans. Transp. Electrific.*, vol. 9, no. 1, pp. 622–630, Mar. 2023.

[5] H. Dhulipati, E. Ghosh, S. Mukundan, P. Korta, J. Tjong, and N. C. Kar, "Advanced design optimization technique for torque profile improvement in six-phase PMSM using supervised machine learning for direct-drive EV," *IEEE Trans. Energy Convers.*, vol. 34, no. 4, pp. 2041–2051, Dec. 2019.

[6] J. Hao, S. Suo, Y. Yang, Y. Wang, W. Wang, and X. Chen, "Optimization of torque ripples in an interior permanent magnet synchronous motor based on the orthogonal experimental method and MIGA and RBF neural networks," *IEEE Access*, vol. 8, pp. 27202–27209, 2020.

[7] B. Yan, Y. Yang, and X. Wang, "Design of a large capacity line-start permanent magnet synchronous motor equipped with hybrid salient rotor," *IEEE Trans. Ind. Electron.*, vol. 68, no. 8, pp. 6662–6671, Aug. 2021.

[8] Z. Zheng, J. Zhao, L. Wang, F. Dong, and X. Yang, "Efficient optimization design method of PMSLM based on deep adaptive ridge regression with embedded analytical mapping function," *IEEE Trans. Ind. Electron.*, vol. 69, no. 8, pp. 8243–8254, Aug. 2022.

[9] Z. Pan and S. Fang, "Torque performance improvement of permanent magnet arc motor based on two-step strategy," *IEEE Trans. Ind. Inform.*, vol. 17, no. 11, pp. 7523–7534, Nov. 2021.

[10] M.-S. Kwon and D.-K. Lim, "A study on the optimal design of PMa-SynRM for electric vehicles combining random forest and genetic algorithm," *IEEE Access*, vol. 11, pp. 52357–52369, 2023.

[11] S. Barmada, N. Fontana, L. Sani, D. Thomopulos, and M. Tucci, "Deep learning and reduced models for fast optimization in electromagnetics," *IEEE Trans. Magn.*, vol. 56, no. 3, Mar. 2020, Art. no. 7513604.

[12] H. Sasaki, Y. Hidaka, and H. Igarashi, "Prediction of IPM machine torque characteristics using deep learning based on magnetic field distribution," *IEEE Access*, vol. 10, pp. 60814–60822, 2022.

[13] H. Sato and H. Igarashi, "Deep learning-based surrogate model for fast multi-material topology optimization of IPM motor," *COMPEL - Int. J. Comput. Math. Elect. Electron. Eng.*, vol. 41, no. 3, pp. 900–914, 2022.

[14] A. Khan, C. Midha, and D. Lowther, "Reinforcement learning for topology optimization of a synchronous reluctance motor," *IEEE Trans. Magn.*, vol. 58, no. 9, Sep. 2022, Art. no. 8206204.

[15] Y. Shimizu, S. Morimoto, M. Sanada, and Y. Inoue, "Using machine learning to reduce design time for permanent magnet volume minimization in IPMSMs for automotive applications," *IEEJ J. Ind. Appl.*, vol. 10, no. 5, pp. 554–563, 2021.

[16] Y. Shimizu, "Efficiency optimization design that considers control of interior permanent magnet synchronous motors based on machine learning for automotive application," *IEEE Access*, vol. 11, pp. 41–49, 2023.

[17] Y. Shimizu, S. Morimoto, M. Sanada, and Y. Inoue, "Automatic design system with generative adversarial network and convolutional neural network for optimization design of interior permanent magnet synchronous motor," *IEEE Trans. Energy Convers.*, vol. 38, no. 1, pp. 724–734, Mar. 2023.

[18] Y. Shimizu, "Dataset for iron losses of IPMSMs," IEEE Dataport, Aug. 19, Paper OC2-3-379, 2022, doi: 10.21227/18kr-b698.

[19] Y. Shimizu, "Investigation of iron loss prediction model for automatic design system of IPMSMs," in *Proc. 24th Int. Conf. Comput. Electromagn. Fields*, 2023.

[20] M. Farhadian, M. Moallem, and B. Fahimi, "Multimodal optimization algorithm for torque ripple reduction in synchronous reluctance motors," *IEEE Access*, vol. 10, pp. 26628–26636, 2022.

[21] J.-C. Son, J.-Y. Kim, J.-W. Choi, D.-K. Lim, and H.-K. Yeo, "Performance enhancement of the IPMSM for HEV applications using grain-oriented electrical steel and design optimization," *IEEE Access*, vol. 10, pp. 46599–46607, 2022.

[22] S. Das et al., "Sensitivity analysis based NVH optimization in permanent magnet synchronous machines using lumped unit force response," *IEEE Trans. Ind. Appl.*, vol. 58, no. 3, pp. 3533–3544, May/Jun. 2022.

[23] P.-D. Pfister, C. Tang, and Y. Fang, "A multi-objective finite-element method optimization that reduces computation resources through subdomain model assistance, for surface-mounted permanent-magnet machines used in motion systems," *IEEE Access*, vol. 11, pp. 8609–8621, 2023.

[24] Y. Shimizu, S. Morimoto, M. Sanada, and Y. Inoue, "Influence of permanent magnet properties and arrangement on performance of IPMSMs for automotive applications," *IEEJ J. Ind. Appl.*, vol. 6, no. 6, pp. 401–408, Nov. 2017.

[25] S. Suzuki, S. Morimoto, M. Sanada, and Y. Inoue, "Performance comparison of IPMSMs using a low iron loss material for automotive application," in *Proc. 19th Int. Conf. Elect. Mach. Syst.*, 2016, pp. 1–6.

[26] T. Akiba, S. Sano, T. Yanase, T. Ohta, and M. Koyama, "Optuna: A next-generation hyperparameter optimization framework," in *Proc. 25th ACM SIGKDD Int. Conf. Knowl. Discov. Data Mining*, 2019, pp. 2623–2631.

[27] Z. Liu et al., "Swin transformer: Hierarchical vision transformer using shifted windows," in *Proc. IEEE/CVF Int. Conf. Comput. Vis.*, 2021, pp. 9992–10002.

[28] C. P. Steinmetz, "On the law of hysteresis," *Proc. IEEE*, vol. 72, no. 2, pp. 197–221, Feb. 1984.

[29] J. Deng, W. Dong, R. Socher, L.-J. Li, K. Li, and L. Fei-Fei, "ImageNet: A large-scale hierarchical image database," in *Proc. IEEE Conf. Comput. Vis. Pattern Recognit.*, 2009, pp. 248–255.

[30] K. He, X. Zhang, S. Ren, and J. Sun, "Deep residual learning for image recognition," in *Proc. IEEE Conf. Comput. Vis. Pattern Recognit.*, 2016, pp. 770–778.

[31] K. Simonyan and A. Zisserman, "Very deep convolutional networks for large-scale image recognition," in *Proc. Int. Conf. Learn. Representations*, 2015, doi: 10.48550/arXiv.1409.1556.

[32] A. Dosovitskiy et al., "An image is worth 16x16 words: Transformers for image recognition at scale," in *Proc. Int. Conf. Learn. Representations*, 2021, doi: 10.48550/arXiv.2010.11929.

[33] W. Yu et al., "Metaformer is actually what you need for vision," in *Proc. IEEE/CVF Conf. Comput. Vis. Pattern Recognit.*, 2022, pp. 10809–10819.

[34] K. Deb, A. Pratap, S. Agarwal, and T. Meyarivan, "A fast and elitist multiobjective genetic algorithm: NSGA-II," *IEEE Trans. Evol. Comput.*, vol. 6, no. 2, pp. 182–197, Apr. 2002.

[35] J. Blank and K. Deb, "Pymoo: Multi-objective optimization in Python," *IEEE Access*, vol. 8, pp. 89497–89509, 2020.

Yuki Shimizu (Member, IEEE) received the B.E., M.E., and Ph.D. degrees in engineering from Osaka Prefecture University, Sakai, Japan, in 2016, 2018, and 2022, respectively.

In 2018, he joined Toyota Motor Corporation, Aichi, Japan. In 2022, he joined the Graduate School of Science and Engineering, Ritsumeikan University, where he is currently an Assistant Professor. In 2023, he also founded MotorAI, Inc., where he is currently the Chief Executive Officer. His main research interests include the design and control of permanent magnet synchronous motors using machine learning and deep learning.

Dr. Shimizu is a member of the Institute of Electrical Engineers of Japan, the Japan Institute of Power Electronics, and the Society of Automotive Engineers of Japan.